Volume 1 | Number 1 | Jan 2013 | Pages 1–100

Nanoscale

www.rsc.org/nanoscale

ROYAL SOCIETY
OF CHEMISTRY

ROYAL SOCIETY
OF CHEMISTRY

www.rsc.org/nanoscale

Nanoscale

ARTICLE

High interfacial storage capability of porous NiMn$_2$O$_4$/C hierarchical tremella-like nanostructures as lithium ion battery anode

Wenpei Kang[a], Yongbing Tang[a,b]*, Wenyue Li[b,a], Xia Yang[a], Hongtao Xue[a], Qingdan Yang[a], and Chun-Sing Lee[a]*

Porous hierarchical NiMn$_2$O$_4$/C tremella-like nanostructures are obtained through a simple solvothermal and calcination method. As anode of lithium ion batteries (LIBs)**,** the porous NiMn$_2$O$_4$/C nanostructure exhibits superior specific capacity, excellent long-term cycling performance even at a high current density. The discharge capacity can stabilize at 2130 mAh g^{-1} within 350 cycles at a current density of 1000 mA g^{-1}. After long-term cycling of 1500 cycles, the capacity is still as high as 1773 mA h g^{-1} at a high current density of 4000 mA g^{-1}, which is almost five times higher than the theoretical capacity of graphite. The porous NiMn$_2$O$_4$/C hierarchical nanostructure provides sufficient contact with electrolyte and fast three-dimensional Li$^+$ diffusion channels, and dramatically improves the capacity of NiMn$_2$O$_4$/C via interfacial storage.

1. Introduction

Hierarchical nanostructures or superstructures have attracted extensive attention owing to the synergistic effects of their nanometer-sized building blocks and overall micrometer-sized structures.[1-6] These hierarchical structures not only provide characteristic size effects, they also give desirable mechanical strength, facile ion transportation and easy recycling. They are considered promising candidates for applications in high performance energy conversion and storage devices,[7-12] catalysts,[11-13] and adsorbents.[14,15] These hierarchical structures are also important for electrode materials for lithium ion batteries (LIBs) and exhibit superior electrochemical performances because of their unique properties comparing with their bulk counterparts. [16-19]

As an important spinel binary metal oxide, NiMn$_2$O$_4$ has been applied in many fields, such as magnetism,[20,21] catalysis,[22] negative temperature coefficient thermistors,[23] sensors,[24] supercapacitor, etc.[25,26] NiMn$_2$O$_4$ nanostructures have been synthesized by various methods including solid-state reaction,[27] co-precipitation,[28] sol–gel,[29] and microemulsion-mediated routes.[21] Additionally, precursor method has been widely used to prepare binary metal oxides such as ZnMn$_2$O$_4$, CoMn$_2$O$_4$, NiMn$_2$O$_4$, and CuMn$_2$O$_4$, etc.[30-35] Porous NiMn$_2$O$_4$ nanostructures have been successfully prepared using oxalate precursor,[21,25] and exhibit improved electrochemical performance due to their porous characteristic. As anode candidates of LIBs, nanostructured transition metal oxides have attracted much attention for their merits of high surface-to-volume ratio and short path length for Li-ion diffusion.[36-41] Particularly, binary metal oxides have been among the most widely investigated alternative anode materials because of their much higher specific capacities ($\sim$ 1000 mA h g^{-1}) comparing to that of conventional graphite (372 mA h g^{-1}).[42-45] Among these oxides, Mn-based oxides AMn$_2$O$_4$ (M=Co, Zn, Mn) exhibit excellent anodic performance. Lou's group reported a capacity of 750 mA h g^{-1} in ZnMn$_2$O$_4$ after 120 cycles,[30] and a capacity of 624 mA h g^{-1} in CoMn$_2$O$_4$ after 50 cycles.[31] CoMn$_2$O$_4$ anode was also reported to have a capacity of 706 mA h g^{-1} after 25 cycles by Xiong's group.[17]

Considering that nanostructured nickel-based oxides are also electrochemically active and can contribute to the lithium storage capability, we studied the electrochemical performances of Ni-containing Mn-based oxide as an anode material for LIBs. Recent studies showed that hierarchical geometries especially porous nanostructures can significantly increase capacities of oxide anode materials due to interfacial lithium storage as reported by Maier et al and re-oxidization to a higher oxidation state upon cycling.[46-51] Herein, we report a porous NiMn$_2$O$_4$/C hierarchical tremella-like nanostructure assembled with nanoparticles via a simple solvothermal and calcination method for LIB application. This porous hierarchical nanostructure effectively facilitates Li$^+$ ion transport by decreasing the diffusion distance and accommodates volume changes during charging/discharging processes. As anode of LIB, this tremella-like nanostructure exhibits a stable capacity of $\sim$2130 mAh g^{-1} at a high current density of 1000 mA g^{-1} after 350 cycles. Moreover, it still retains a capacity of $\sim$1773 mAh g^{-1} even at a higher current density of 4000 mA g^{-1} after 1500 cycles, indicating its potential applications for LIBs with long cycle life and high power density.

2. Experimental

2.1 Preparation of NiMn$_2$O$_4$/C

All reagents were used as received. Typically, 0.5 mmol of Ni(CH$_3$COO)$_2$·4H$_2$O, 1.0 mmol of Mn(CH$_3$COO)$_2$·2H$_2$O and 3 mmol of hexamethylenetetramine were dissolved into a mixed solvent of 5.0 mL water and 25.0 mL triethylene glycol (TEG). The above solution was then transferred into a Teflon-lined stainless steel autoclave and held at 180°C for 16 h. After naturally cooled to room temperature, precursor precipitate was collected by centrifugation, washed several times with deionized water and ethanol, and vacuum dried at 60°C for 12 h. The obtained precursor was mixed with polyacrylonitrile (PAN) at a weight ratio of 5:1 in a solvent of N, N-dimethylformamide and then dried at 150 °C on a hot plate. To obtained the final product of NiMn$_2$O$_4$/C, the above mixture was first calcinated at 250 °C in air for 3 h and then at 600 °C in N$_2$ for 3 h.

2.2 Materials characterization

X-ray diffraction (XRD) measurements were carried out on a Siemens D-500 diffractometer using Cu Ka radiation. Scanning electron microscopy (SEM) and transmission electron microscopy (TEM) were respectively carried out with a Philips XL30 FEG SEM and a Philips FEG TEM CM200 (operated at 200 kV). X-ray photoelectron spectroscopy (XPS) analysis was performed in a VG ESCALAB 220i-XL UHV surface analysis system with a monochromatic Al Kα X-ray source (1486.6 eV). Thermogravimetric analyzer (TGA) measurement was performed under air atmosphere at a heating rate of 10 °C min^{-1} from room temperature to 600°C. Fourier transform infrared spectroscopy (FTIR) measurements were performed on a VERTEX-70 spectrometer using the KBr tablet method.

2.3 Electrochemical measurements

Working electrodes were prepared by mixing NiMn$_2$O$_4$/C with acetylene black and sodium alginate at a weight ratio of 5:3:2 and with a total weight loading of 1.2 ± 0.3 mg cm^{-2}. LiPF$_6$ solution (1 mol L^{-1}) in an ethylene carbonate and dimethyl carbonate mixture (1:1, v/v) was used as the electrolyte. Galvanostatic cycling tests were measured using a Macco Instruments system. Cyclic voltammetry (CV) measurements were carried out over a potential window of 0.01-3.0 V with an electrochemical workstation (CHI 660D). Electrochemical impedance spectroscopy (EIS) was carried out on a ZAHNER-elektrik IM6 over a frequency range of 100 kHz to 10 mHz.

3. Results and Discussion

Tremella-like carbonate precursor was obtained with the described solvothermal process. To obtain the desired bimetallic salt, instead of a mixture of the two monometallic salts, the processing conditions have to be optimized such that the solubility of the desired bimetallic salt should be lower than those of the individual monometallic salts.[21] To realize this, polyol is usually used in the solvothermal reaction.[52-54] In our studies, the mixture of TEG and water (5:1, V/V) was used as the solvent for the preparation of the binary metal carbonate precursor with tremella-like nanostructures. A series of control experiment has also been carried out to emphasize the

importance of solvent (Fig. S1, S2) and the raw materials of acetate (Fig. S3) on the formation of carbonate precursor with the tremella-like nanostructures.
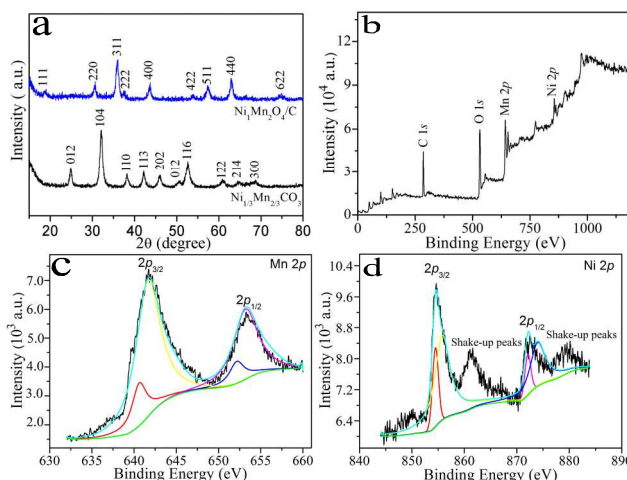

Fig. 1 (a) XRD patterns of NiMn$_2$O$_4$/C and its precursor Ni$_{1/3}$Mn$_{2/3}$CO$_3$; XPS spectra for the as-prepared NiMn$_2$O$_4$ nanostructure: (b) a survey spectrum, (c) a Mn 2p and (d) a Ni 2p core level spectra.

The bottom curve of Fig. 1a shows XRD patterns of the as-prepared precursor. All the peaks can be well indexed based on the standard XRD patterns of MnCO$_3$ (JCPDS No. 86-0173) and NiCO$_3$ (JCPDS No. 78-0210). Together with the energy dispersive spectroscopy (EDS) analysis (Fig. S4), the precursor can be confirmed as Ni$_{1/3}$Mn$_{2/3}$CO$_3$. After mixed with PAN and calcinated at 600°C, all the diffraction peaks in the XRD patterns (the top curve in Fig. 1a) of the obtained sample can be assigned to well-crystallized cubic spinel NiMn$_2$O$_4$ (JCPDS No. 84–0542). Oxidation state of the corresponding transition metal ions in the obtained sample is further investigated with X-ray photoelectron spectroscopy (XPS). A survey spectrum (Fig. 1b) shows the presence of Ni, Mn, and O as well as C and there is no other impurity. A Mn 2p core level spectrum (Fig. 1c) shows two major peaks with binding energies of 641.7 and 653.2 eV, assigned to the Mn 2p$_{3/2}$ and Mn 2p$_{1/2}$ peaks, respectively.[17] After refined fitting, the spectrum composes of four peaks. Those with binding energies of 641.8 eV and 653.3 eV are ascribed to Mn^{3+}. Another two peaks at 640.7 eV and 652.3 eV are ascribed to Mn^{2+}. Similarly, the Ni 2p spectrum (Fig. 1d) shows two spin-orbit doublets characteristics of Ni^{2+} and Ni^{3+} states and shake-up peaks at around 861.2 and 879.7 eV at the high binding energy side of the Ni 2p$_{3/2}$ and Ni 2p$_{1/2}$ edge.[55,56] The fitted peaks at 854.5 and 872.1 eV are attributed to Ni^{2+}, while the other peaks at 855.8 and 874.0 eV are related to Ni^{3+}. According to the XPS analyses, the couples of Mn^{3+}/Mn^{2+} and Ni^{3+}/Ni^{2+} are coexisting in the spinel NiMn$_2$O$_4$ nanostructures. The atomic ratio of Ni and Mn is ~1:2 based on the areas of their corresponding XPS peaks.

Fig. 2a displays SEM images of the as-prepared Ni$_{1/3}$Mn$_{2/3}$CO$_3$ precursor. It can be seen that the precursor has a tremella-like hierarchical morphology assembled by many nanoplatelets as shown in the inset of Fig. 2a. It was found that morphology of the obtained precursor depends strongly on the reaction solvent. Only irregular aggregates composed of small particles can be formed if water was used as the solvent (Fig. S1). Meanwhile, if the solvent is pure TEG, the obtained precursor shows non-uniform feather-like structures (Fig. S2a,

2b). Star-like structures can be obtained in a solvent of TEG and water with a ratio of 1:1 (Fig. S2c, 2d). TEM observations indicated that the carbonate precursor can be well dispersed (Fig. 2b), and many nanoplatelets were integrated into a tremella-like hierarchical structure (inset of Fig. 2b).
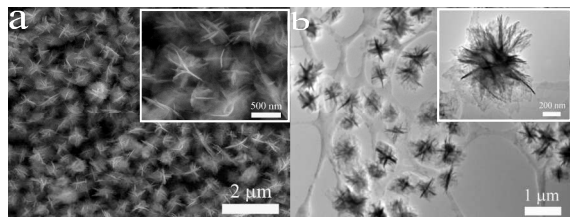

Fig. 2 (a) SEM and (b) TEM images of the $Ni_{1/3}Mn_{2/3}CO_3$ precursor. The insets are the corresponding magnified images.

To get more insight into the actual evolution process of the tremella-like precursor structure, a series of time-dependent experiments were performed, and intermediate products were obtained at different reaction intervals (Fig. S5). The XRD patterns indicate that the carbonate precursor forms from the initial reaction stage and the crystallinity increases along with the reaction time. The sequential SEM images reveal a morphological evolution from random particles to the coexistence of particles and flakes, then the coexistence of particles, flakes and flake aggergate, and finally to the 3D hierarchical tremella-like nanostructures. We propose a precipitation-dissolution-recrystallization-oriented aggregation mechanism to explain the formation of the $Ni_{1/3}Mn_{2/3}CO_3$ tremella-like structure. Finally, after calcination, porous $NiMn_2O_4/C$ nanostructures can be obtained. Preparation of the tremella-like hierarchical structure is schematically illustrated in Fig. 3.

Fig. 3 Schematic diagram for the formation of $Ni_{1/3}Mn_{2/3}CO_3$ tremella-like structure and porous $NiMn_2O_4/C$ nanostructures.

After calcination with PAN, the precursors transformed into porous $NiMn_2O_4/C$ tremella-like nanostructures, as shown in Fig. 4. It should be noted that after mixed with PAN, the hierarchical tremella-like structures are thermally stable, while the structures collapse after heat treatment without using PAN (Fig. S6). Additionally, the calcination treatment with PAN deposit non-uniform carbon films (marked with white arrows) on the tremella-like nanostructures as shown in Fig. 4a and 4b, which is beneficial for LIB applications. As the contrast of the carbon films differ considerably from that of the $NiMn_2O_4$ nanostructures, it is difficult to simultaneously show their images clearly. We have adjust the contrast of Fig. 4a and 4b, such that the carbon films can be more clearly shown in Fig. S7. Meanwhile, the tremella-like nanostructure becomes porous and composed of numerous nanoparticles as shown in the inset of Fig. 4b. EDS microanalysis of the $NiMn_2O_4/C$ hierarchical tremella-like structures is shown in Fig. S8. The nanostructures were found to contain only Ni, Mn, O and C, and the ratio of Ni and Mn is about 1:2, further confirming the formation of pure

$NiMn_2O_4$. Also the C content is shown by FTIR and estimated to be 0.75 wt% based on the TGA analysis (Fig. S9). In addition, energy dispersive x-ray spectroscopy mapping (Fig. S10) show the homogeneity of Ni, Mn and O in the tremella-like structures. The porous characteristic of the $NiMn_2O_4/C$ hierarchical nanostructures was further examined via TEM observations (Fig. 4c). Brunauer–Emment–Teller (BET) analysis of the porous $NiMn_2O_4/C$ tremella-like structures gives a specific surface area of 38.9 m^2 g^{-1}, a pore volume of 0.237 cm^3 g^{-1} as shown in Fig. S11. In addition, an SAED pattern (the inset in Fig. 4c) of the $NiMn_2O_4$ nanostructure shows its polycrystalline nature. An HRTEM image (Fig. 4d) shows lattice fringes with interplanar spacing of 0.233, 0.204 and 0.289 nm corresponding to the (222), (400) and (220) planes of the spinel $NiMn_2O_4$ phase, respectively
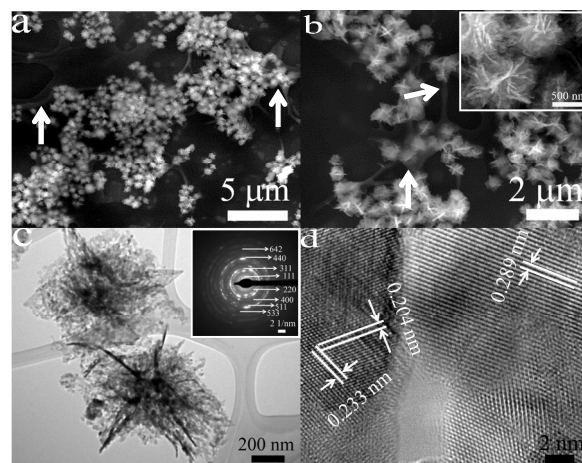

Fig. 4 (a, b) SEM images, (c) TEM image and (d) HRTEM image of the porous $NiMn_2O_4/C$ tremella-like nanostructures; the inset in panel (b) is the magnified SEM image; and the inset in panel (c) is the corresponding SAED pattern.

Electrochemical performance of the tremella-like $NiMn_2O_4/C$ hierarchical nanostructures as anode material for LIB was first investigated by cyclic voltammetry (CV). Fig. 5a shows the first five CV curves of the $NiMn_2O_4/C$ electrode at a scanning rate of 0.2 mV s^{-1} over the voltage range of 0.01-3.0 V. In the first cycle, the broad peak between 0.30-0.90 V can be attributed to the reduction of $NiMn_2O_4$ to Mn and Ni. In the anodic process, two broad oxidation peaks located at ~1.25 V and ~1.96 V, are ascribed to the oxidation of Mn to Mn^{3+} and Ni to Ni^{2+}.[17, 57] In the second cycle, the cathodic peaks at 1.02 and 0.53 V correspond to the reduction of Mn^{3+} to Mn^{2+} and Mn^{2+} or Ni^{2+} to metallic Mn or Ni, respectively. In the following cycles, the redox peaks move to lower potentials, while the anodic peaks show little changes. Apparently, the differences in the second cycle indicate a different electrochemical mechanism from the first anodic process. For the following cycles, the CV curves are almost overlapped, implying excellent electrochemical reversibility. Based on the above CV analysis, the electrochemical reactions for the $NiMn_2O_4$ electrode can be summarized as follows: [17, 57]

$$NiMn_2O_4 + 8Li^+ + 8e^- \rightarrow Ni + 2Mn + 4Li_2O \quad (1)$$
$$Ni + Li_2O \leftrightarrow NiO + 2Li^+ + 2e^- \quad (2)$$
$$Mn + Li_2O \leftrightarrow MnO + 2Li^+ + 2e^- \quad (3)$$
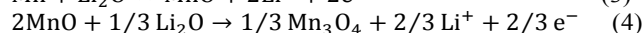$$2MnO + 1/3\,Li_2O \rightarrow 1/3\,Mn_3O_4 + 2/3\,Li^+ + 2/3\,e^- \quad (4)$$
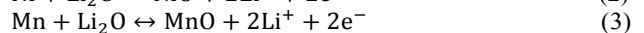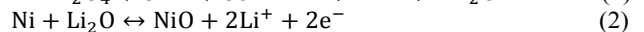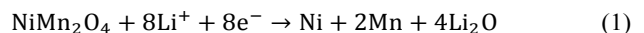
Fig. 5b shows typical discharge-charge curves of the LIB with the $NiMn_2O_4$/C tremella-like anode at 1000 mA g^{-1} over a voltage range of 0.01-3.0 V. The initial discharge capacity is 1617 mA h g^{-1} with a corresponding Coulombic efficiency (CE) of 62.8%. The 37.2% capacity loss is mainly attributed to the formation of solid electrolyte interphase (SEI) during the first discharge process.[58] The discharge capacities in the 2nd and 150th cycles are 997 and 979 mA h g^{-1}, respectively, which are both higher than the theoretical value (~922 mA h g^{-1}) of $NiMn_2O_4$. The high capacities could be attributed to synergistic effects, including the reversible formation/dissolution of polymeric gel-like film resulted from electrolyte degradation,[59-63] which is often observed in transition metal oxides, and the insertion of lithium ions into interfacial storage[46,47] and acetylene black.[64]
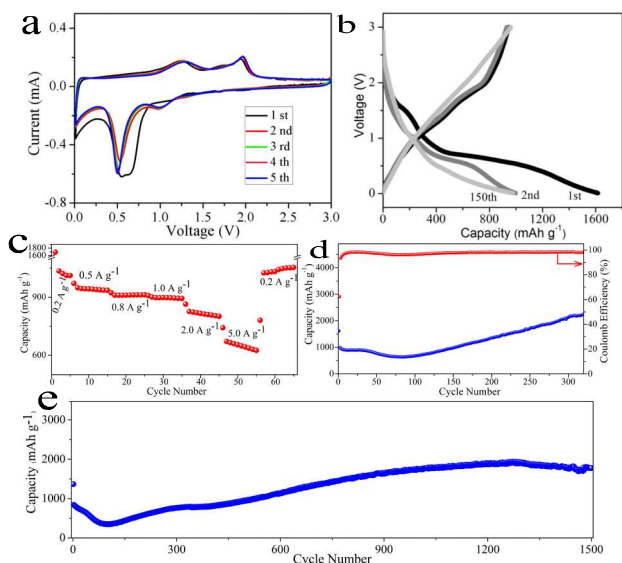

improve the electrochemical performance based on the fact of preserving the hierarchical structure and providing a continuous pathway for electron transport.To further evaluate the cycle stability of the $NiMn_2O_4$/C nanostructure electrode, we test the long-term cycling performance at a much higher current density of 4000 mA g^{-1}. As shown in Fig. 5e, the capacity also shows a similar trend compared with that at a current density of 1000 mA g^{-1}. The electrode retains its capacity very well for 1500 cycles. The capacity in the 1500th cycle is still as high as 1773 mA h g^{-1}, which is almost five times higher than the theoretical capacity of graphite.
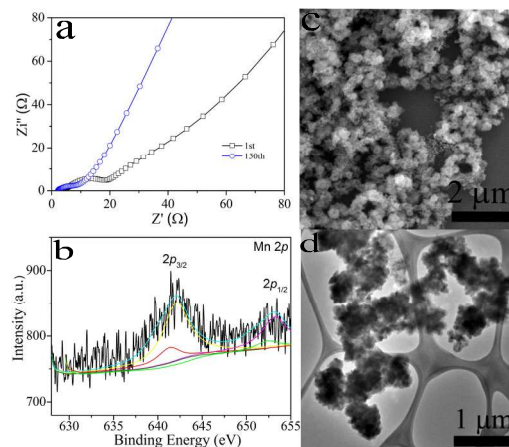

Fig. 6 (a) Nyquist plots in the range of 100 kHz to 10 mHz of $NiMn_2O_4$/C electrode at a full discharge state after different cycles at 1000 mA g^{-1}; (b) Mn 2p XPS spectrum of the $NiMn_2O_4$/C electrode in a full charge state after 350 cycles at 1000 mA g^{-1}; (c) SEM and (d) TEM images of the $NiMn_2O_4$/C nanostructures electrode observed after 350 discharge/charge cycles at 1000 mA g^{-1}.

Fig. 5 (a) CV curves at a scan rate of 0.2 mV s^{-1} over the voltage range of 0.0-3.0 V, (b) Representative charge–discharge curves at a current density of 1000 mA g^{-1}, (c) Rate capability, (d) Cycling performance at current density of 1000 mA g^{-1}, and (e) long-term cycling at a high current density of 4000 mA g^{-1} for the as-prepared tremella-like $NiMn_2O_4$/C hierarchical nanostructure electrode.

The porous $NiMn_2O_4$/C tremella-like structure electrode also exhibits remarkable rate performance (Fig. 5c). Upon cycling at current densities of 200, 500, 800, 1000, 2000 and 5000 mA g^{-1}, the porous $NiMn_2O_4$/C nanostructure electrode shows discharge capacities of 1035, 948, 909, 900, 826 and 671 mAh g^{-1}, respectively. The capacity can be retained to 1025 mA h g^{-1} as the current density reduces back to 200 mA g^{-1}, indicating a good rate-cycling stability of this nanostructure. Long-term cycling performance of the porous $NiMn_2O_4$/C nanostructures was also measured at high current densities of 1000 mA g^{-1} and 4000 mA g^{-1} (Fig. 5d, 5e). At a current density of 1000 mA g^{-1}, after the first cycle, the discharge capacity shows almost stable capacities of ~900 mAh g^{-1} in the initial 30 cycles with the CE around ~98%. Then the capacity decreases to a value of 680 mAh g^{-1} within 100 cycles. After that, it is interesting that the capacity increase gradually and can reach a high value of 2130 mAh g^{-1} after 300 cycles and then keep almost stable within 350 cycles. However, the pristine $NiMn_2O_4$ nanoparticles only show continuously decreasing capacities (Fig. S12). So a small amount of the doped C can

The porous $NiMn_2O_4$/C tremella-like nanostructure in this work exhibits a superior electrochemical performance compared with other binary transition metal oxides for LIBs. The high capacity of this porous nanostructure should be attributed to the continuously reversible formation of a polymeric gel-like film originating from the progressive kinetic activation in the electrode. Similar phenomenon has also been reported by Maier et al.[46] They pointed out that the interfacial storage is mainly from the reversible formation/dissolution of organic polymeric gel-like layer by electrolyte decomposition, which could deliver an extra capacity through a so-called pseudo-capacitive behavior. In each discharge process fresh metal surface is generated due to the conversion characteristic of TMOs, and so additional electrolyte decomposition is need to form SEI films. The electrolyte can thus penetrate into inner part of the porous hierarchical nanostructures after several cycles. As a result, the inner part of the nanostructures is gradually involved in the conversion reactions and leads to the increased capacity. Nyquist plots of the electrode for the 1st and 150th cycles are shown in Fig. 6a. The charge-transfer resistance for the 150th cycle (~3 Ω) was obviously smaller than that in the 1st cycle (~7 Ω), which indicates the activation and improved kinetics upon cycling. In addition, through XPS analysis of the Mn peaks for the electrode material in the full charge state after 350 cycles at 1000 mA g^{-1} in the Fig. 6b, we can observe the characteristic peak for Mn^{4+} at about 653.3 eV and 642.2 eV, while these peaks cannot be observed in the as prepared $NiMn_2O_4$/C. This suggests that some Mn^{2+} or Mn^{3+}

ions can be re-oxidized to a higher oxidation state (e.g. Mn^{4+}) upon cycling, which also leads to an increasing capacity according to Huang's report.[50]

To understand the relationship between the improved performances and structure, we also study the morphology changes of the porous $NiMn_2O_4/C$ tremella-like nanostructure electrode upon cycling (Fig. 6c, 6d). After 350 discharge/charge cycles at 1000 mA g^{-1}, the tremella-like nanostructures changed into porous clusters (Fig. 6c) composed of many nanosized particles, promoting the surface Li storage capacities, and thus lead to a capacity increase during the discharge process.[46] On the other hand, although the tremella-like morphology changed upon cycling, the porous characteristic of the formed clusters still provide sufficient contact with electrolyte and three-dimensional channels for Li$^+$ diffusion (Fig. 6d), which should be contributed to the long life capacity stability of this porous $NiMn_2O_4/C$ tremella-like hierarchical nanostructure.

4. Conclusions

Porous tremella-like $NiMn_2O_4/C$ hierarchical nanostructures can be facilely obtained through thermal annealing treatment of the synthesized $Ni_{1/3}Mn_{2/3}CO_3$ precursor with a carbon source of PAN. As anode material, porous the $NiMn_2O_4/C$ nanostructure electrode shows a superior high capacity of 2130 mAh g^{-1} within 350 cycles at current density of 1000 mA g^{-1}. Even at a high current of 4000 mA g^{-1}, the capacity can reach as high as 1773 mA h g^{-1} mAh g^{-1} after 1500 cycles, which is almost five times higher than the theoretical capacity of graphite. The excellent electrochemical performance can be attributed to the porous hierarchical structures of $NiMn_2O_4/C$ with a specific surface area of 38.9 m^2 g^{-1}, which is in favor of the interfacial lithium storage state upon cycling. The further oxidation of transition metal to higher oxidization states can also contribute to the increased capacity. It is believe that the high rate capacity and cycling stability of this porous $NiMn_2O_4/C$ nanostructure will make it promising anode candidate for high performance LIB applications.

Acknowledgements

Notes and references

a Department of Physics and Materials Science and Center of Super-Diamond and Advanced Films (COSDAF), City University of Hong Kong, Hong Kong SAR, People's Republic of China.
b Functional Thin Films Research Center, Shenzhen Institutes of Advanced Technology, Chinese Academy of Sciences, People's Republic of China.
*Corresponding author.
E-mail: tangyb@siat.ac.cn; apcslee@cityu.edu.hk; Tel: +852-34427826

1   S. J. Guo and E. K. Wang, *Nano Today*, 2011, **6**, 240.

2   J. Jiang, Y. Y. Li, J. P. Liu, X. T. Huang, C. Z. Yuan and X. W. Lou, *Adv. Mater.*, 2012, **24**, 5166.

3   C. Z. Yuan, H. B. Wu, Y. Xie and X. W. Lou, *Angew. Chem. Int. Ed.*, 2014, **53**, 1488.

4   J. J. Wu, W. P. Liao and M. Yoshimura, *Nano Energy*, 2013, **2**, 1354.

5   Y. Li, Z. Y. Fu and B. L. Su, *Adv. Funct. Mater.*, 2012, **22**, 4634.

6   C. M. A. Parlett, K.Wilson and A. F. Lee, *Chem. Soc. Rev.,* 2013, **42**, 3876.

7   S. Jin, H. Deng, D. Long, X. Liu , L. Zhan, X. Liang, W. Qiao and L. Ling, *J. Power Sources*, 2011, **196**, 3887.

8   D. W. Liu, B. B. Garcia, Q. F. Zhang, Q. Guo, Y. H. Zhang , S. Sepehri and G. Z. Cao, *Adv. Funct. Mater.*, 2009, **19**, 1015.

9   T. Y. Wei, C. H. Chen, H. C. Chien, S. Y. Lu and C. C. Hu, *Adv. Mater.*, 2010, **22**, 347.

10 Z. Yang , Y. Xia and R. Mokaya, *J. Am. Chem. Soc.*, 2007, **129**, 1673.

11 L. Xu, S. Sithambaram, Y. Zhang, C. H. Chen, L. Jin, R. Joesten and S. L. Sui, *Chem. Mater.*, 2009, **21**, 1253.

12 M. Prabu, K. Ketpang and S. Shanmugam, *Nanoscale*, 2014, **6**, 3173.

13 Y. F. Zhao, M. Wei, J. Lu, Z. L.Wang and X. Duan, *ACS Nano*, 2009, **3**, 4009.

14 X. Y. Yu, T. Luo, Y. Jia, R. X. Xu, C. Gao, Y. X. Zhang, J. H. Liu and X. J. Huang, *Nanoscale*, 2012, **4**, 3466.

15 L. H. Ai, H. T. Yue and J. Jiang, *Nanoscale*, 2012, **4**, 5401.

16 L. L. Wang, W. Cheng, H. X. Gong, C. H. Wang, D. K. Wang, K. B. Tang and Y. T. Qian, *J. Mater. Chem.,* 2012, **22**, 11297

17 J. F. Li, S. L. Xiong, X. W. Li and Y. T. Qian, *Nanoscale*, 2013, **5**, 2045.

18 S. L. Xiong, J. S. Chen, X. W. Lou and H. C. Zeng, *Adv. Funct. Mater.*, 2012, **22**, 861.

19 W. P. Kang and Q. Shen, *J. Power Source*, 2013, **238**, 203.

20 M. Tadic, S. M. Savic, Z. Jaglicic, K. Vojisavljevic, A. Radojkovic, S. Prsic and D. Nikolic, *J. Alloys Compd.*, 2014, **588**, 465.

21 Menaka, N. Garg, S. Kumar, D. Kumar, K. V. Ramanujachary, S. E. Loflandc and A. K. Ganguli, *J. Mater. Chem.*, 2012, **22**, 18447

22 S. Fritsch, J. Sarrias, M. Brieu, J. J. Couderc, J. L. Baudour, E. Snoeck and A. Rousset, *Solid State Ionics*, 1998, **109**, 229.

23 D. Mehandjiev, E. Zhecheva, G. Ivanov and R. Ioncheva, *Appl. Catal. A: Gen.*, 1998, **167**, 277.

24 D. L. Fang, Z. B. Wang, P. H. Yang, W. Liu and C. S. Chen, *J. Am. Ceram. Soc.*, 2006, **89**, 230.

25 H. Pang, J. W. Deng, S. M. Wang, S. J. Li, J, M. Du, J. Chen and J. S. Zhang, *RSC Adv.*, 2012, **2**, 5930.

26 M. Zhang, S. H. Guo, L. Zheng, G. N. Zhang, Z. P. Hao, L. P. Kang and Z. H. Liu, *Electrochim. Acta*, 2013, **87**, 546.

27 W. H. Cloud, *Phys. Rev.*, 1958, 111, 1043.

28 A. Ashcroft, I. Terry and R. Gover, *J. Eur. Ceram. Soc.,* 2006, **26**, 901.

29 J. M. A. Almeida, C. T. Meneses, A. S. de Menezes, R. F. Jardim and J. M. Sasaki, *J. Magn. Magn. Mater.*, 2008, **320**, 304.

30 G. Q. Zhang, L. Yu, H. B. Wu, H. E. Hoster and X. W. Lou, *Adv. Mater.*, 2012, **24**, 4609.

31 L. Zhou, D. Y. Zhao and X. W. Lou, *Adv. Mater.*, 2012, **24**, 745.

32 L. Zhou, H. B. Wu, T. Zhu and X. W. Lou, *J. Mater. Chem.*, 2012, **22**, 827.

33 G. Fortunato, H. R. Oswald and A. Reller, *J. Mater. Chem.*, 2001, **11**, 905.

34 F. M. Courtel, Y. Abu-Lebdeh and I. J. Davidson *Electrochim. Acta*, 2012, **71**, 123.

35 F. M. Courtel, H. Duncan, Y. Abu-Lebdeh and I. J. Davidson, *J. Mater. Chem.*, 2011, **21**, 10206

36 Y. G. Wang, H. Q. Li, P. He, E. Hosono and H. S. Zhou, *Nanoscale*, 2010, **2**, 1294.

37 P. Poizot, S. Laruelle, S. Grugeon, L. Dupont and J. M. Tarascon, *Nature*, 2000, **407**, 496.

38 J. Jiang, Y. Y. Li, J. P. Liu, X. T. Huang, C. Z. Yuan and X. W. Lou, *Adv. Mater.*, 2012, **24**, 5166.

39 M. V. Reddy, G. V. Subba Rao and B. V. R. Chowdari, *Chem. Rev.*, 2013, **113**, 5364.

40 W. M. Zhang, X. L. Wu, J. S. Hu, Y. G. Guo and L. J. Wan, *Adv. Funct. Mater.*, 2008, **18**, 3941.

41 Z. S. Wu, W. C. Ren, L. Wen, L. B. Gao, J. P. Zhao, Z. P. Chen, G. M. Zhou, F. Li and H. M. Cheng, *ACS Nano*, 2010, **4**, 3187.

42 J. Y. Wang, N. L. Yang, H. J. Tang, Z. H. Dong, Q. Jin, M. Yang, D. Kisailus, H. J. Zhao, Z. Y. Tang and D. Wang, *Angew. Chem. Int. Ed.*, 2013, **52**, 6417.

43 R. Alcá̈ntara, M. Jaraba, P. Lavela and J. L. Tirado, *Chem. Mater.*, 2002, **14**, 2847.

44 S. H. Choi and Y. C. Kang, *ChemSusChem.*, 2013, **6**, 2111.

45 L. Yu, L. Zhang, H. B. Wu, G. Q. Zhang and X. W. Lou, *Energy Environ Sci.*, 2013, **6**, 2664.

46 J. Maier, *Nat. Mater.*, 2005, **4**, 805.

47 P. Balaya, H. Li, L. Kienle and J. Maier, *Adv. Funct. Mater.*, 2003, **13**, 621.

48 V. Augustyn, P. Simonbc and B. Dunn, *Energy Environ. Sci.*, 2014,**7**, 1597.

49 J. F. Li, J. Z. Wang, X. Liang, Z. J. Zhang, H. K. Liu, Y. T. Qian and S. L. Xiong, *ACS Appl. Mater. Interfaces*, 2014, **6**, 24.

50 Y. M Sun, X. L. Hu, W. Luo , F. F. Xia and Y. H. Huang, *Adv. Funct. Mater.*, 2013, **23**, 2436.

51 S. Luo, H. C. Wu, Y. Wu , K. L. Jiang, J. P. Wang and S. S. Fan, *J. Power Sources*, 2014, **249**, 463.

52 W. P. Kang, C. H. Zhao, R. Liu, F. F. Xu and Q. Shen, *CrystEngComm*, 2012, **14**, 2245.

53 Y. L. Wang, X. C. Jiang and Y. N. Xia, *J. Am. Chem. Soc.*, 2003, **125**, 16176.

54 Y. C. Qiu, S. H. Yang, H. Deng, L. M. Jin and W. S. Li, *J. Mater. Chem.*, 2010, **20**, 4439.

55 J. F. Marco, J. R. Gancedo, M. Gracia, J. L. Gautier, E. I. Rı´os, H. M. Palmer, C. Greaves and F. J. Berry, *J. Mater. Chem.*, 2001, **11**, 3087.

56 B. Cui, H. Lin, Y. Z. Liu, J. B. Li, P. Sun, X. C. Zhao and C. J. Liu, *J. Phys. Chem. C*, 2009, **113**, 14083.

57 L. L. Li, Y. Y. Cheah, Y. Ko, P. F. Teh, G. Wee, C. L. Wong, S. J. Peng and M. Srinivasan, *J. Mater. Chem. A*, 2013, **1**, 10935.

58 W. P. Kang, F. L. Liu, Y. L. Su, D. J. Wang and Q. Shen, *CrystEngComm*, 2011, **13**, 4174.

59 R. Demir-Cakan, Y. S. Hu, M. Antonietti, J. Maier and M. M. Titirici, *Chem. Mater.*, 2008, **20**, 1227.

60 H. Wang , L. F. Cui , Y. Wang, H. S. Casalongue, J. T. Robinson, Y. Liang, Y. Cui and H. Gai, *J. Am. Chem. Soc.*, 2010, **132**, 13978.

61 B. Z. Jang, C. Liu, D. Neff, Z. Yu, M. C. Wang, W. Xiong and A. Zhamu, *Nano Lett.*, 2011, **11**, 3785.

62 S. W. Lee, N. Yabuuchi, B. M. Gallant, S. Chem, B. S. Kim, P. T. Hammond and Y. Shao-Horn, *Nat. Naonotechnol.*, 2010, **5**, 531.

63 H. C. Liu and S. K. Yen, *J. Power Sources*, 2007, **166**, 478.

64 Y. Deng, Q. Zhang, S. Tang, L. Zhang , S. Deng, Z. Shi and G. Chen, Chem. Commun., 2011, **47**, 6828.